ORNL/TM-9689

Dist. Category UC-20 g

Fusion Energy Division

# ATF NEUTRAL BEAM INJECTION: OPTIMIZATION OF BEAM ALIGNMENT AND APERTURING

R. N. Morris and R. H. Fowler Computing and Telecommunications Division

J. A. Rome and T. J. Schlagel
Fusion Energy Division

This report was prepared as an account of work sponsored by an agency of the United States Government. Neither the United States Government nor any agency thereof, nor any of their employees, makes any warranty, express or implied, or assumes any legal liability or responsibility for the accuracy, completeness, or usefulness of any information, apparatus, product, or process disclosed, or represents that its use would not infringe privately owned rights. Reference herein to any specific commercial product, process, or service by trade name, trademark manufacturer, or otherwise does not necessarily constitute or imply its endorsement, recommendation, or favoring by the United States Government or any agency thereof. The view and opinions of authors expressed herein do not necessarily state or reflect those of the United States Government or any agency thereof.

DATE PUBLISHED - December 1985



NOTICE: This document contains information of a preliminary nature. It is subject to revision or correction and therefore does not represent a final report.

Prepared by
OAK RIDGE NATIONAL LABORATORY
Oak Ridge, Tennessee 37831
operated by
MARTIN MARIETTA ENERGY SYSTEMS, INC.
for the
U.S. DEPARTMENT OF ENERGY
under Contract No. DE-AC05-84OR21400

DISCLAIME

# CONTENTS

ACKNOV	VLED	GME	NT	S	•	•	•		•	•		•	•	•	•	•	•	•	•	•	•	•	•	•	V
ABSTRA	CT .			•			•			•			•					•			•				vii
1. INTRO	DUC'	MOI1	1				•	•				•	•									•	•		1
2. THE P	HYSI	CS N	10D	EL			•	•			•	•	•	•											5
3. COMP	UTEL	RE	SUI	TS	•								•												7
4. FAST-I	ON C	ONF	'INI	CME	N'	r				•	•		•	•						•	•				18
5. CONC	LUSIC	NS			•					•	•		•						•		•		•		<b>2</b> 0
REFERE	NCES	•								•				•					•	•	•				21
APPEND	IX A:	CO	ORI	OIN	AT.	ΕN	ÆΙ	PI	NG						•		•								23
A PPENID	TY D.	BE A	M	MO	יונו	7 T	רעי	/CT/	70																25

# **ACKNOWLEDGMENTS**

The authors wish to thank M. M. Menon for many useful discussions about the neutral beam apparatus and its physical modeling. We also thank G. H. Neilson for his help in reviewing this manuscript. Sam Hokin orginally adapted the deposition code to stellator geometry.

## 1. INTRODUCTION

The success of the Advanced Toroidal Facility (ATF) depends upon the ability of the external heating source to effectively heat the contained plasma without introducing impurities into the plasma. The primary heating source for the initial operation of ATF will be neutral beam injection, which has been very successful to date in experiments on tokamaks and stellarators. However, injection into ATF presents unique problems because of its complex vacuum vessel and plasma shapes.

The two issues to be addressed are beam line aiming and beam aperturing. Beam line aiming is the process of aligning the optical axis of the beam line so that the beam is directed to a desired location in the plasma. Beam aperturing is the process of stopping a portion of the beam by placing an obstruction in the beam path; this beam shaping is necessary to prevent the beam particles from striking some undesired location in the beam line port or the vacuum vessel. A schematic view of the injection geometry at the ATF vacuum vessel midplane is shown in Fig. 1, with the angles  $\theta_1$  and  $\theta_2$  being the primary beam-aiming angles. The details of the neutral beam injector model used in the simulation are shown in Fig. 2. The actual beam-aiming angles that deliver the most power to the plasma have been determined empirically using a particle-following Monte Carlo simulation. The computer program used is an upgrade of the Oak Ridge NFREYA beam injection code with major modifications to the geometric portion and to the Cartesian-to-flux coordinate conversion subroutines (see Appendixes A and B for details about the physics modeling). 1-3 The problem of aiming the beam may be conceptualized as the problem of fitting a cone (because of beam divergence) into the ATF vacuum vessel with the apex of the cone pointing out through the port toward the source. The problem is further complicated by the fact that the beam is attenuated as it travels through the plasma, making "fitting" of the cone more important at the "apex" end than at the base end (because of lower beam intensity at that point).

Figure 3 is a phantom view of the injection port as seen by the neutral beam aiming point. The solid polygonal shape is the vacuum vessel port, the structure to the right of center is the helical coil trough, and the circular arc to the left of and outside the port is the vacuum vessel wall near the beam tangency point. The helical coil trough is the region that is in danger of being struck by the "apex" of the beam divergence cone, while the vessel wall near the tangency point may be struck by the "base" of the cone. Note that because of the coil trough the beam is pushed over to the left side of the injection port; any further migration to the left, however, will result in an increased beam flux on the near tangency region, in addition to a significant fraction of the beam missing the port.

After aligning the beam for maximum deposition into the plasma, the beam is then apertured to minimize particle interception by the vacuum vessel and vacuum vessel port. In general, the

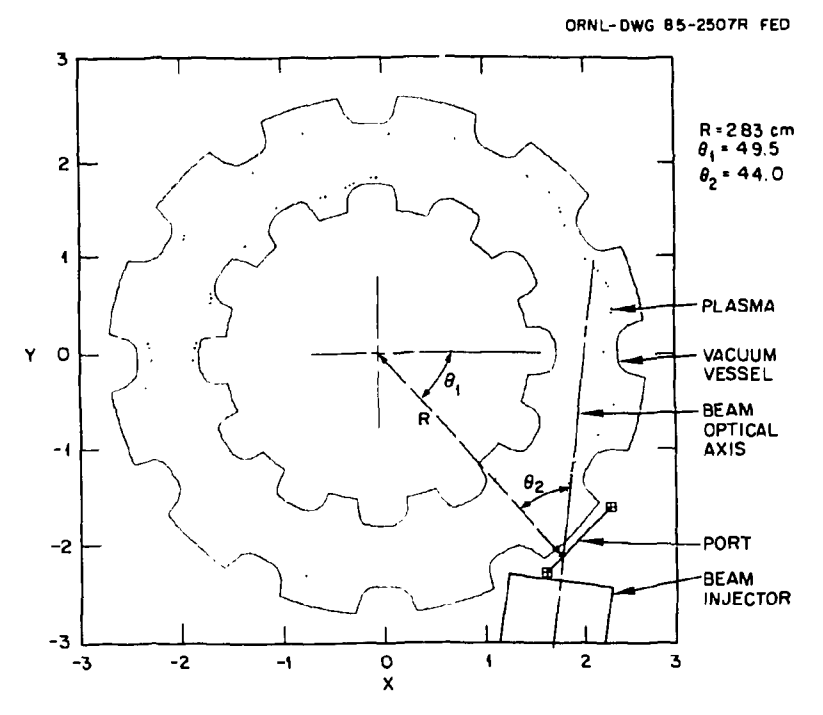


Fig. 1. Schematic view of the injector geometry at the vacuum vessel midplane.

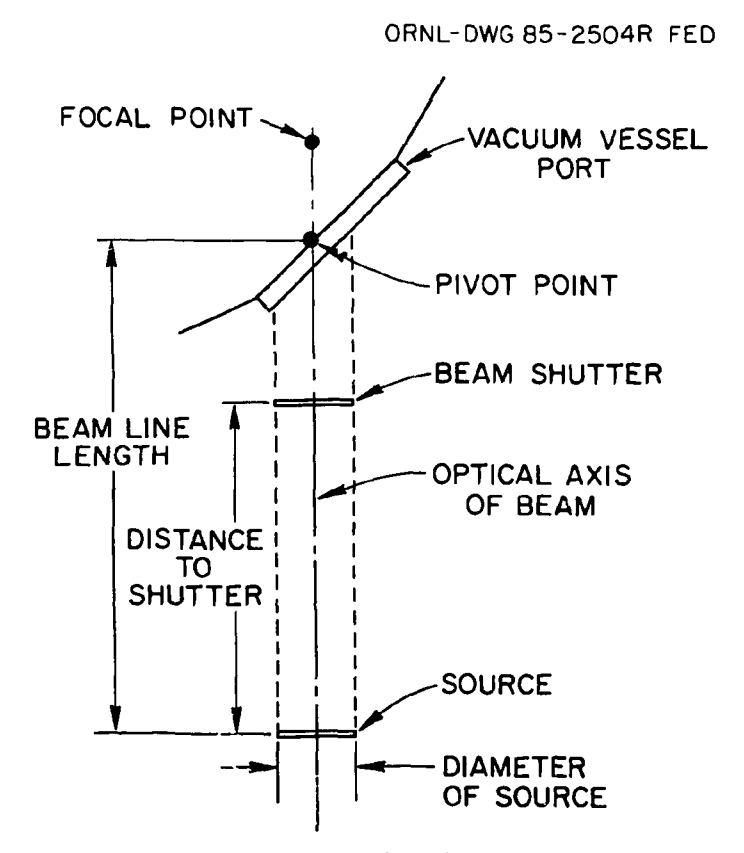
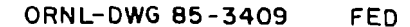


Fig. 2. Neutral beam physics injection model.



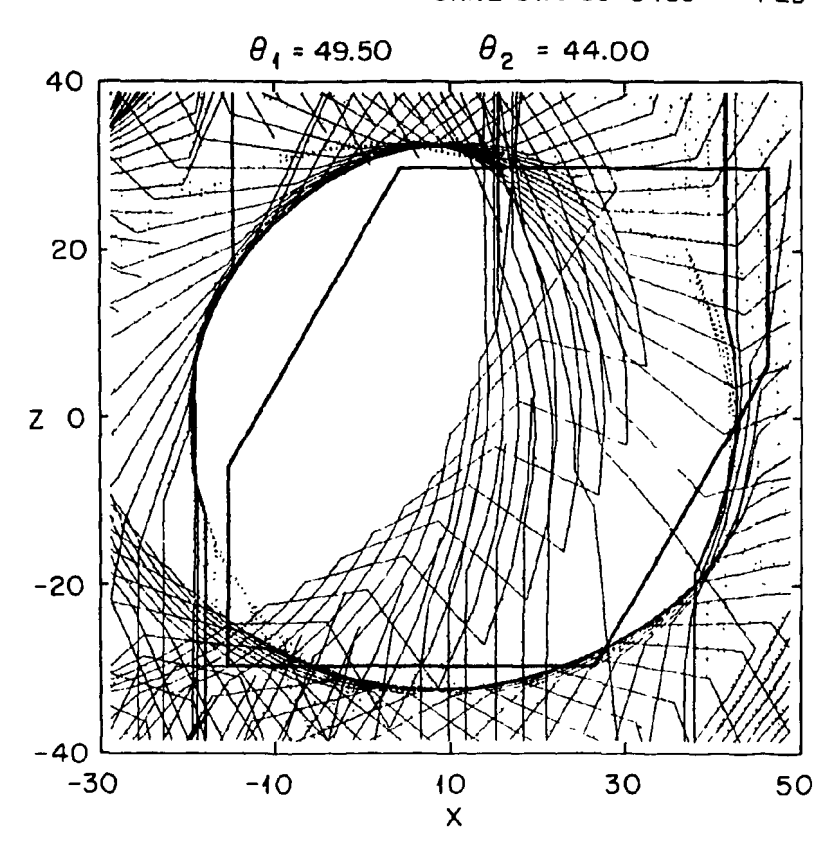


Fig. 3. Phantom view of the injection port as seen by the neutral beam aiming point. The solid polygonal shape is the vacuum vessel port, the structure to the right is the helical coil trough, and the circular arc outside the port is the vacuum vessel at the tangency point.

aperturing process results in a significant reduction in the deposited power, and compromises between power deposition in the plasma and wall heating must be made.

To obtain maximum performance in ATF, the injection geometry must be carefully optimized because the injectors themselves were optimized for the Impurity Study Experiment (ISX-B) tokamak, which had different geometrical requirements. Three geometrical requirements for successful neutral beam injection were considered. First, the beam must not damage the vacuum vessel; the power density of the beam is high enough to cause local melting. On the other hand, if a large portion of the beam must be apertured off to avoid vacuum vessel damage, the resulting beam power may be insufficient to achieve the planned goals. The second requirement is that a large fraction of the injected power be deposited within the central plasma region for efficient heating. The third requirement is that beam-induced impurities must be low.

The optimization depends not only on the geometric constraints posed by the vacuum vessel shape, but also on the specific modeling used for the neutral beam representation. This work presents the results for two types of beam profile modeling, the Gaussian and bi-Gaussian models. A beam model is taken to be Gaussian if the particle perpendicular angular distribution function can be modeled as a simple Gaussian; bi-Gaussian if the function is represented as the sum of two such Gaussians with different exponents (see Appendix B). The Gaussian model forms the basis of the majority of the previous work and provides a first approximation to the beam.<sup>1-2</sup> The bi-Gaussian model is an effort to more closely model a measured beam profile, specifically the beam "tails." The two models can produce significantly different results, and care must be taken to apply the correct representation.

The goal of this work is to compare the power deposited within the plasma to the total power available from the output of the neutral beam injector as a function of beam focal length, divergence, and aperture size. Also of interest is the wall power loading as a function of these parameters and as a function of plasma density for low-density startups. Primary interest has been placed upon the simple Gaussian model, but the final portion of this work demonstrates that this model may not be sufficient and that future work may need to concentrate on the bi-Gaussian representation.

### 2. THE PHYSICS MODEL

The computer model functions by launching a large number of particles into the beam port and following them through their respective physical processes to determine the number that are absorbed in the plasma, are blocked by an aperture, or strike a wall. A brief description of the computer program is presented below.

The delivery of a particle from the neutral beam source to its final location (either a birth point in the plasma or the vacuum vessel wall) is as follows; first, a particle is generated at the source (see Fig. 2) with randomly determined coordinates and velocities chosen from a Gaussian or bi-Gaussian distribution about the normal according to the desired beam model. It is then translated to the plane of the beam shutter. If the particle is within the opening of the shutter, it continues its path to the port; if not, it is stopped by the shutter and its lifetime ended. The surviving particles are further advanced to the vacuum vessel port where, again, those that lie within the port opening are advanced into the vacuum vessel, and those that do not are terminated.

Once within the vacuum vessel, the particles are advanced a distance determined by their local mean free path and then participate in a pseudo collision. As a particle's trajectory is followed in global x,y,z coordinates, a coordinate transformation to flux coordinates, in this case Boozer coordinates,  $^{6.7}$  must be accomplished to determine the plasma parameters. This process is outlined in Appendix A. Once the necessary plasma parameters have been obtained, a call to a random number generator (a "pseudo collision") determines if the particle has been ionized by charge exchange or electron impact. If so, its life is ended and its ionization point recorded. If not, the particle proceeds until it either is ionized or strikes the wall. This process is repeated for approximately 3000 particles.

The vacuum vessel is modeled by a series of cross sections taken at 1° increments in  $\phi$ , the toroidal angle. The particles are stepped along their trajectories in increments that are of the same order as the spacing between the  $\phi$  cross sections. The  $\phi$  value at each step is rounded off to the nearest  $\phi$  cross sectional value, and it is determined if the r and z values of the particle fall within the closed curve representing the vacuum vessel cross section. If they do, the particle continues on to its next step or collision. If not, the particle has struck the wall, and its r, z, and  $\phi$  values are recorded.

This model for the transport of the particle from the injector face to the plasma assumes that if the particle does not strike either the beam shutter or the vacuum vessel port, it will be transported without interference through all beam vacuum chambers and any flanges and vacuum connections. In fact, there could be a considerable loss of beam power in this region, caused by a buildup of neutral gas, which will reionize part of the beam. However, this effect is not accounted for in this model.

The vacuum vessel heating is determined by computing the number of particle strikes and the power deposited within an incremental poloidal arc length of a given vessel cross section and dividing this total by the incremental area. The incremental area is computed by multiplying the above arc length by the toroidal arc length, which is the major radius of the incremental region multiplied by the discretization step in  $\phi$ , 1° in this case. This method is accurate unless  $dr/d\phi$  or  $dz/d\phi$  is very large, as is the case where the transition to the helical field coil cuts occurs. In these cases the power loading is overestimated, because the actual area is larger than the calculated value. This occurs because the incremental arc length along the wall in the quasi-toroidal direction is not approximated by  $rd\phi$ , but by  $(dr^2 + r^2d\phi^2)^{1/2}$  where dr is of the same size as  $rd\phi$ . The structure of the vacuum vessel data made this operation more difficult to perform, and because it occurs for only a few points of interest and yields a conservative answer, more accurate calculations were not pursued. However, if it is desired to operate ATF at near-critical wall loading, this problem should be examined more carefully.

The wall temperature rise,  $T_{rise}$ , for short pulses is modeled by assuming that the vacuum vessel acts as a semi-infinite medium; for short time scale pulses,  $T_{rise}$  is approximately expressed by:

$$T_{\rm rise} = (2q''/k) (\alpha \tau/\pi)^{1/2}$$
,

where q'' is the heat flux (W/cm<sup>2</sup>),  $\alpha$  is the diffusivity (cm<sup>2</sup>/s), k is the thermal conductivity (W/cm·K) and  $\tau$  is the pulse length.<sup>8</sup> The initial temperature of the wall is assumed to be 100°, and the neutral beam pulse length is taken to be approximately 500 ms, which is the maximum possible beam pulse length. This expression is accurate as long as  $\delta^2/\alpha >> \tau$ , where  $\delta$  is the thickness of the vacuum vessel (approximately 0.6 cm). The numerical values used for  $\alpha$  and k are, respectively, 0.0408 and 0.162.

A simple impurity sputtering model was also included in this study, with the sputtered impurities assumed to be produced at a rate proportional to the beam wall flux. Sputtering was assumed to be independent of the angle of incidence, with a production rate of 0.001 ions sputtered for each incidence particle wall hit. This crude model allows one to obtain a rough estimate of the beam-induced impurities near the wall. The sputtering model was not developed beyond this level, as its only purpose was to serve as a guide to aid in the beam-aiming process.

### 3. COMPUTED RESULTS

The optimization of the beam-aiming angles  $\theta_1$  and  $\theta_2$  (see Fig. 1) is determined by first varying  $\theta_1$  and  $\theta_2$  without the beam aperture in place until the beam power deposited within the plasma is maximum. One can then determine the trouble spots. The beam is then apertured and small adjustments made to  $\theta_1$  and  $\theta_2$  to again maximize the power deposited in the plasma while avoiding the trouble spots. In this study no adjustments were made to  $\theta_1$  and  $\theta_2$  when changing between aperture sizes; the angles were set for the largest aperture size. The aiming and aperturing process is an effort to balance the vacuum vessel strikes near the injection point and farther downstream with the power deposited within the plasma.

These angles also show some dependence on the beam energy and species composition. For the most part, this dependence occurs because of the different penetration lengths of different energy particles, with the long-penetration-length particles more likely to strike the vacuum vessel coil troughs farthest from the injection point. These effects may result in minor changes to the aiming angles. A detailed study was not pursued, but the effective change in the deposited power was estimated to be only a percentage or two for minor changes in beam energy and species composition.

The following beam parameters were used in this study (see Fig. 2 for definition of terms):

Beam line length 370 cm Beam input power 4 MW Source current 100 A Beam voltage 40 keV Distance to shutter 320 cm Source diameter 30 cm variable between 1.0° and 1.9° Beam divergence Beam focal length variable between 350 and 500 cm Beam species (by power) 75% 40-keV particles 15% 20-keV particles 10% 13-keV particles Beam species (by number) 37% 40-keV particles 28% 20-keV particles 35% 13-keV particles  $4.0 \times 10^{13} / \text{cm}^3$ Plasma density (on axis)

1 keV

Parabolic (linear in  $\psi$ ).

Temperature (on axis)

Temperature and densities

The beam line efficiency, the ratio between source input power and neutral beam output power, is approximately 68%. Thus, an input power of 4 MW results in about 2.7 MW being delivered to the point just upstream of the beam shutter. In the following text, the percentages given are referenced to the neutral beam power of 2.7 MW. Wallshine is the total energy flux that strikes the inside of the vacuum vessel, and shinethrough is that portion of wallshine that strikes the wall directly downstream from the injection point after traveling through the plasma.

The optimum values for  $\theta_1$  and  $\theta_2$  were found to be 49.5 and 44.0 degrees, respectively; these values remain unchanged for the rest of this report.

The injectors from ISX-B have a focal length of 400 cm and a beam divergence of 1.3°. The beam divergence is defined as the point at which the beam intensity has dropped to the 1/e level with respect to its level on axis, measured in the plane of the beam focal point. All the individual beamlets that make up the total beam are assumed to have the same divergence. With no beam aperturing, approximately 93% of the beam power is deposited within the plasma when using a Gaussian beam model; a typical beam deposition pattern is shown in Fig. 4. About 6% of the beam power strikes the inside of the vacuum vessel, and a smaller amount does not enter the port.

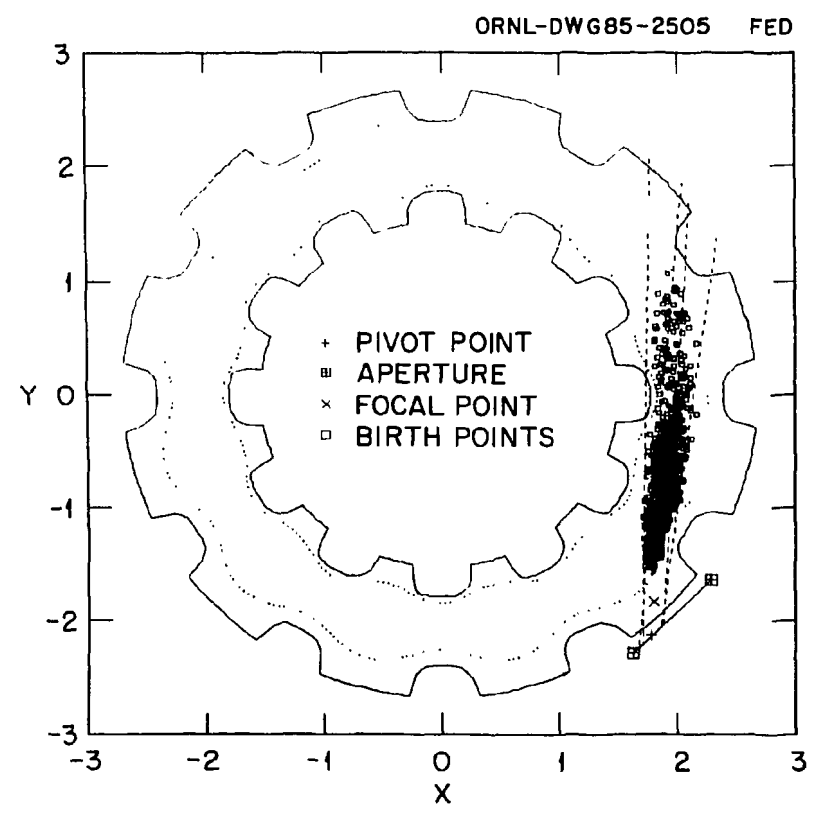


Fig. 4. Birth points for an unapertured 1.3° divergence, 400-cm focal length beam. The vacuum vessel and plasma are shown at their midplanes.

Figure 5 indicates where the particles strike the vacuum vessel, with the vacuum vessel outline in the midplane drawn for reference. Note that the density of impacts (and thus power density) is greatest just inside the port where the cut for the helical coil is made.

Power density calculations indicate that this location is a hot spot. With high-power beam injection (2.7-MW beam power), safe power loading levels will be exceeded. In this application a safe power level is considered to be a maximum of 200 W/cm<sup>2</sup>. As much as 4% of the total input beam power may be deposited in this small region.

In Fig. 6 we plot these vessel particle strikes as a function of  $\theta$  and  $\phi$ , where  $\theta$  is the poloidal angle referenced to zero at the outboard side of the midplane. The helical coil cut clearly shows up at  $-45^{\circ} < \phi < -35^{\circ}$ . At  $-35^{\circ} < \phi < 25^{\circ}$  there is a scatter of hits caused by the beam's skimming the inside of the vacuum vessel; hits between  $\phi = 25^{\circ}$  and  $\phi = 45^{\circ}$  are essentially beam shinethrough. Shinethrough can be reduced exponentially by increasing the plasma density.

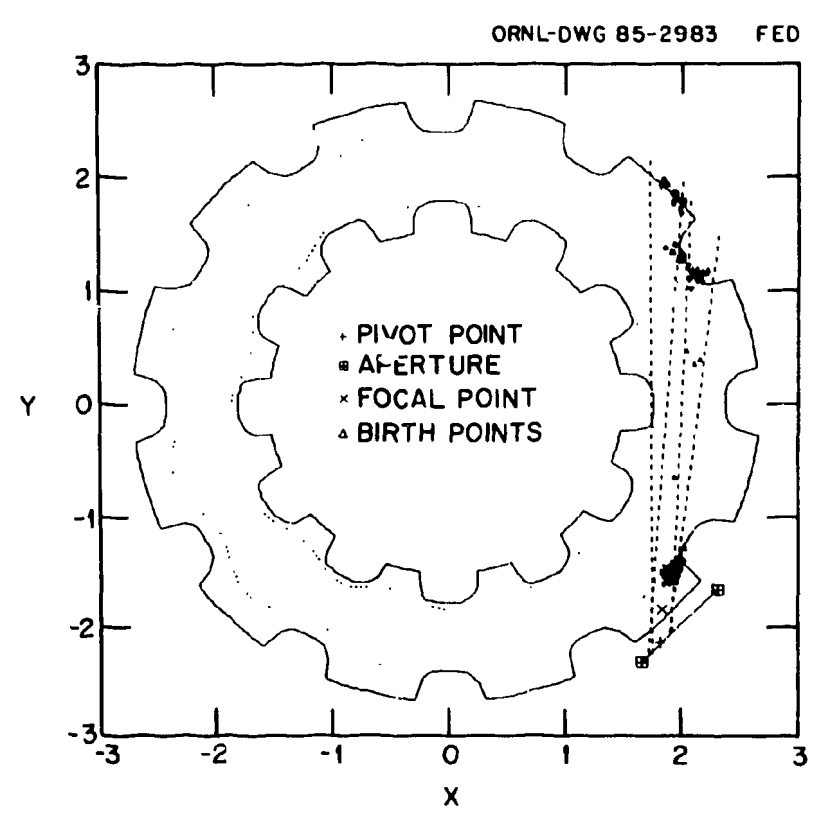


Fig. 5. Vacuum vessel particle strikes for an unapertured 1.3° divergence, 400-cm focal length beam. The vacuum vessel is shown at its midplane; the triangles pointing up indicate hits above the midplane, and those pointing down, hits below the midplane. Note the high density of particle strikes at the coil trough position, the position nearest the injection point.

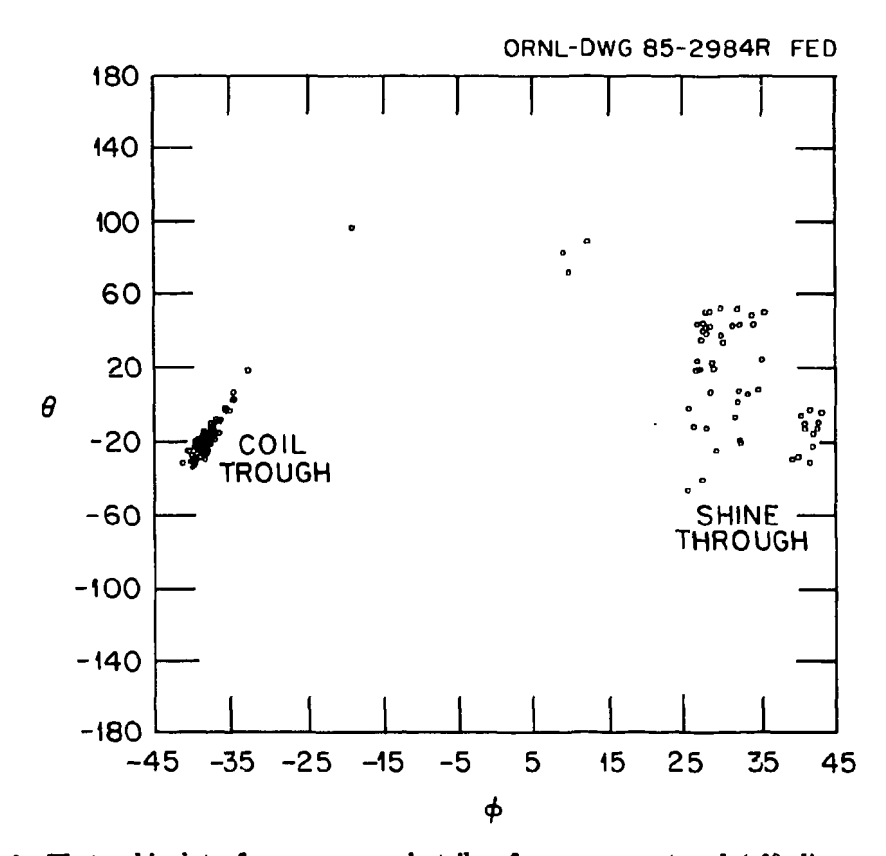
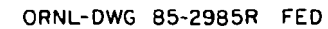


Fig. 6. Theta-phi plot of vacuum vessel strikes for an unapertured 1.3° divergence, 400-cm focal length beam.

In Fig. 7 we plot power density against the toroidal and poloidal angles. The arrows indicate power levels greater than 200 W/cm<sup>2</sup> with an incident beam power of approximately 2.7 MW. The temperature of the vacuum vessel is shown in Fig. 8. The initial temperature was 100°. Figure 9 details the sputtering levels. The worst area is the helical coil trough, with some excessive heating also showing up at the shinethrough region. In addition to the power deposition problem, these regions may also become a source of impurities.

The vacuum vessel power deposition problem may be eliminated by placing an aperture at the position of the beam shutter. If the aperture can be made in a complex shape and placed very close to the vacuum vessel port, it may be possible to solve the vacuum vessel heating problem while minimizing the amount of intercepted beam power. In practice, however, the model provides only an estimate of the actual performance of the beam line, and since the aperture must satisfy many engineering constraints, including vacuum pumping, cooling, and construction, a simple, reliable design is preferred. Because of these demands the beam shutter is located as shown in Fig. 2, and



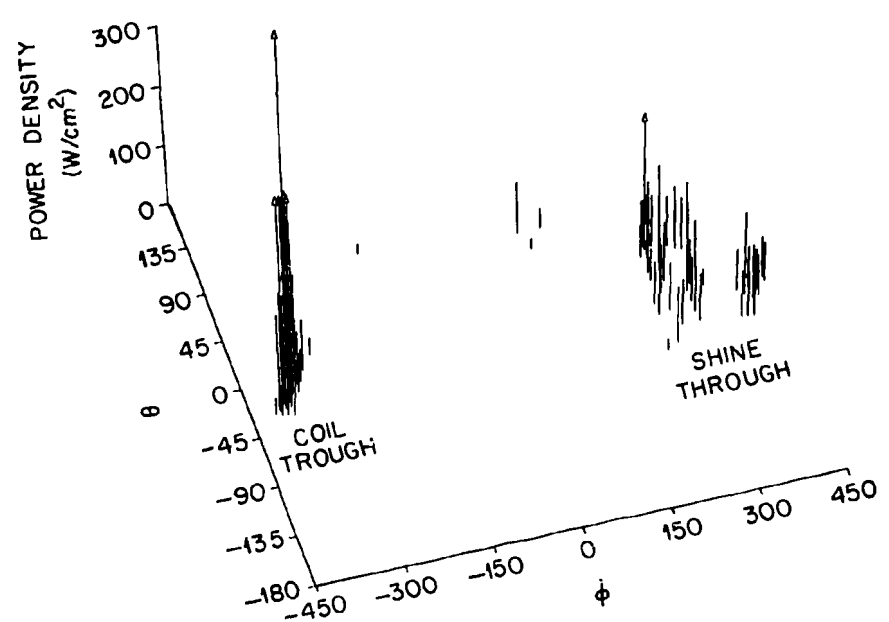


Fig. 7. Power density plot of vacuum vessel strikes for an unapertured 1.3° divergence, 400-cm focal length beam. Arrows lines indicate excessive power density.

•

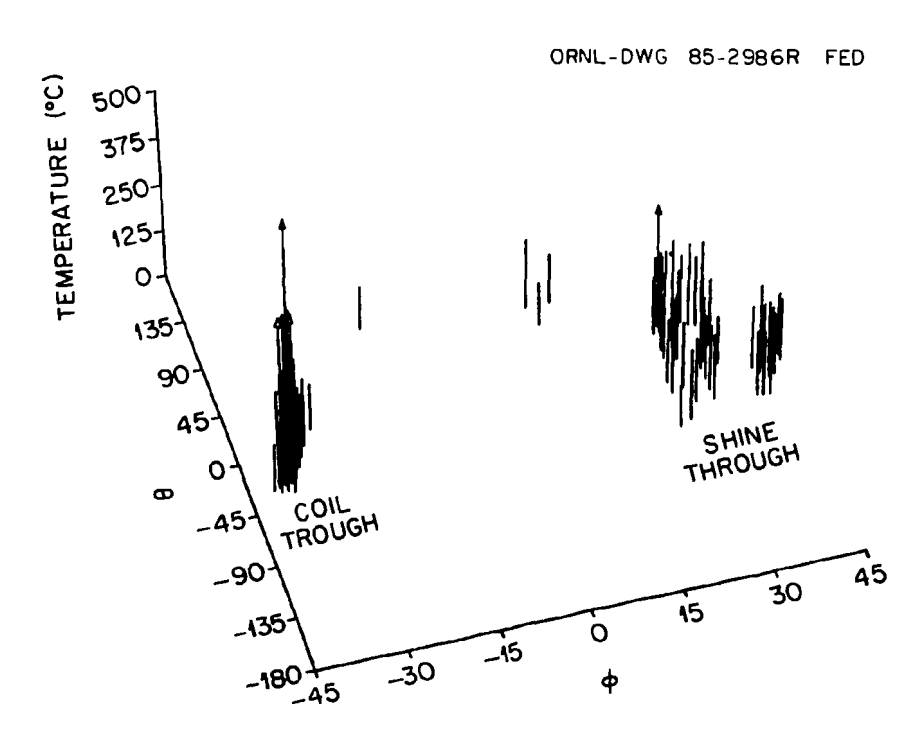


Fig. 8. Vacuum vessel temperature plot for an unapertured  $1.3^{\circ}$  divergence, 400-cm focal length beam.

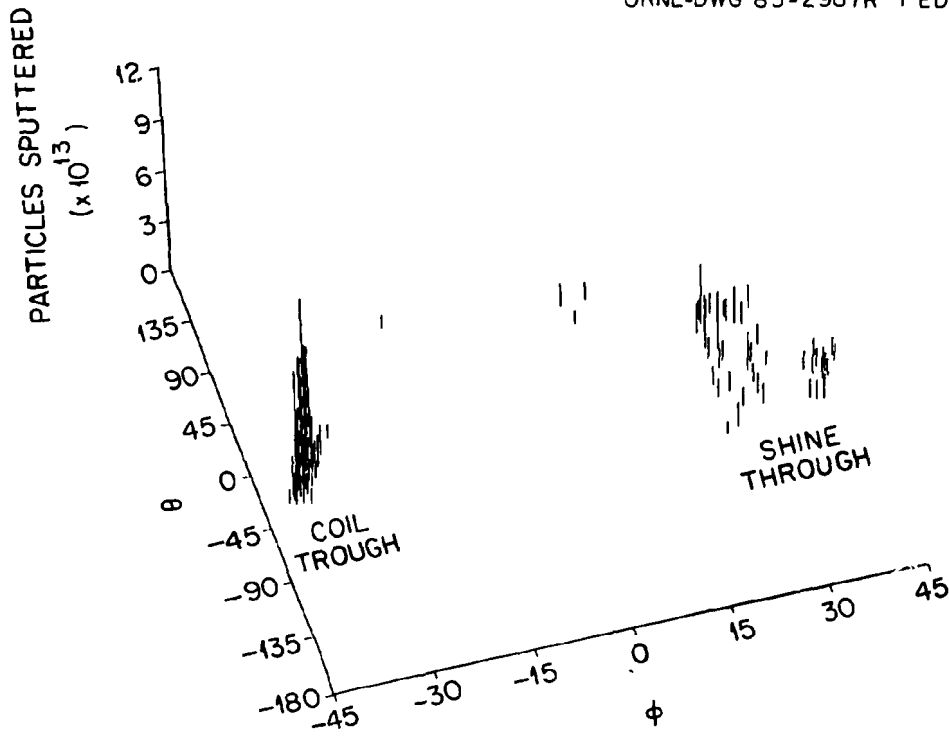


Fig. 9. Sputtering plot for an unapertured 1.3° divergence, 400-cm focal length beam.

its aperture is circular in shape. A diameter of 22 cm was chosen, as this was the maximum diameter consistent with the duct size (30.5 cm) while preventing any beam impacts on the port flanges and ducts. A significantly larger shutter would allow excessive beam strikes on the helical coil trough.

With this change, a modest reduction in the power delivered to the plasma occurs. Figure 10 illustrates the percentage of beam power deposited vs aperture size. The apertured ISX-B injector can deliver about 82% of the beam power (Gaussian model) to the plasma with the 22-cm aperture. Note that even with an 18-cm aperture, more than 70% of the beam energy is deposited within the plasma.

Figures 11 and 12 show the effects of beam divergence and focal length, respectively. Note that the beam divergence is the most critical parameter, with focal length having only a weak influence.

If startup at low densities is required [electron cyclotron heating (ECH) plasma formation], serious shinethrough problems occur. Figure 13 plots power deposition and wallshine vs peak plasma density. Below about  $2 \times 10^{13}$  cm<sup>-3</sup> the shinethrough increases rapidly, and beam energy may have to be reduced to prevent heating and impurity problems. Alternatively, pellet injection or gas puffing can be used to create a more dense target plasma, if startup sources other than ECH were used.

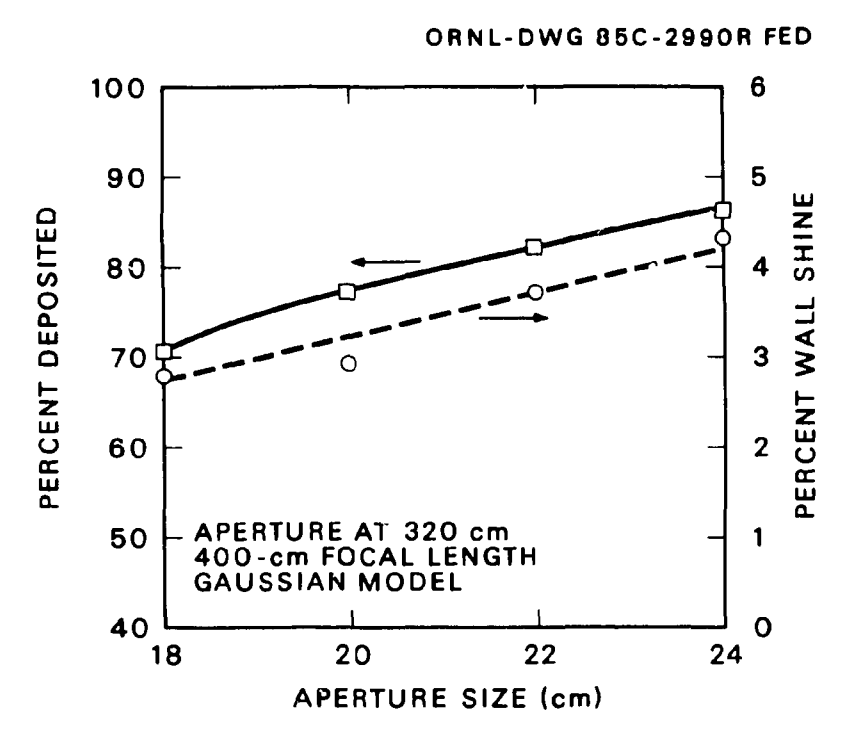


Fig. 10. Power deposited and wallshine vs aperture size for a 1.3° divergence, 400-cm focal length beam.

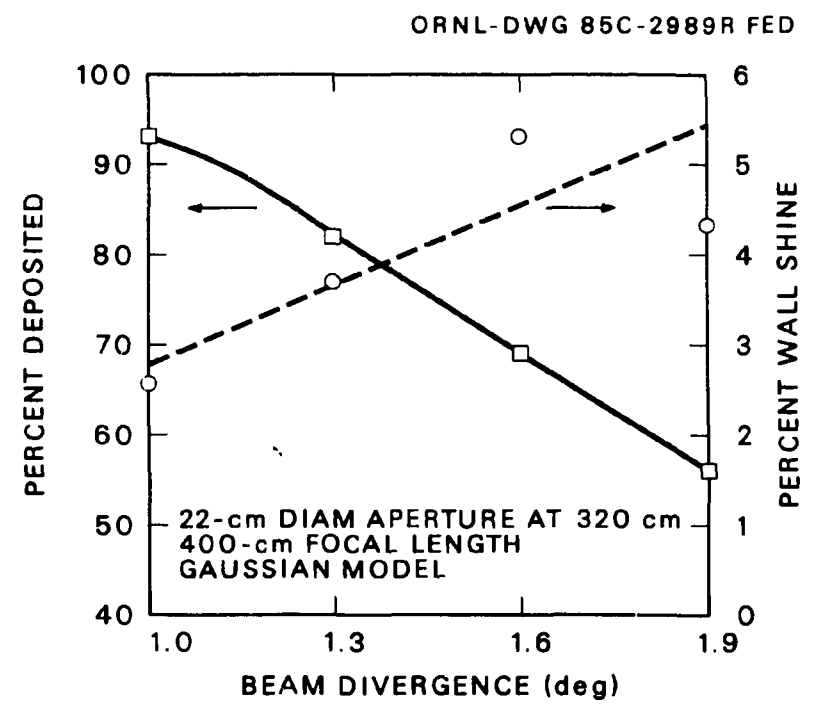


Fig. 11. Power deposited and wallshine vs beam divergence for a 400-cm focal length beam.

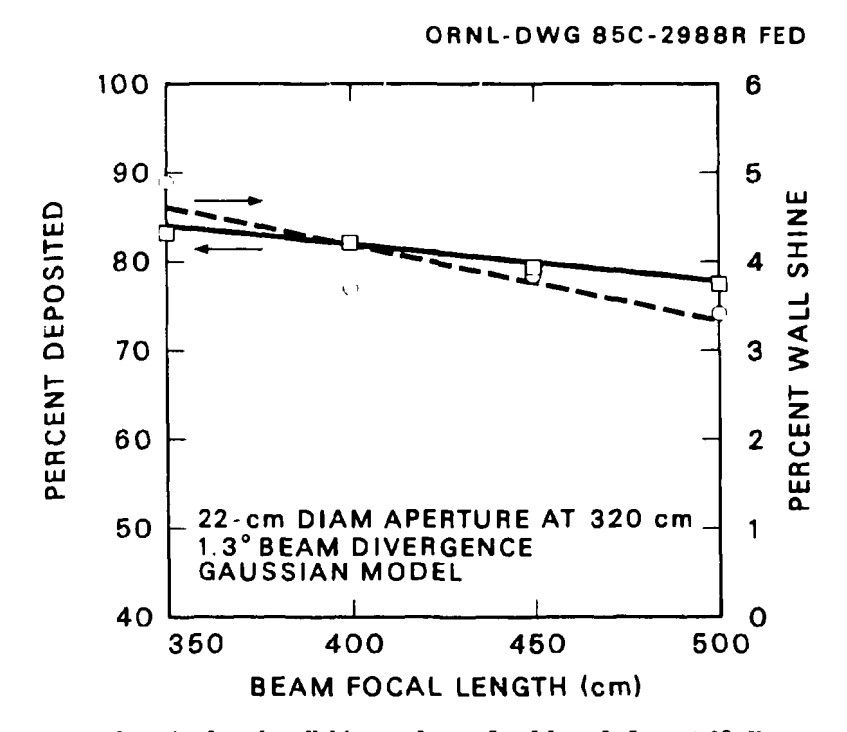


Fig. 12. Power deposited and wallshine vs beam focal length for a 1.3° divergence beam.

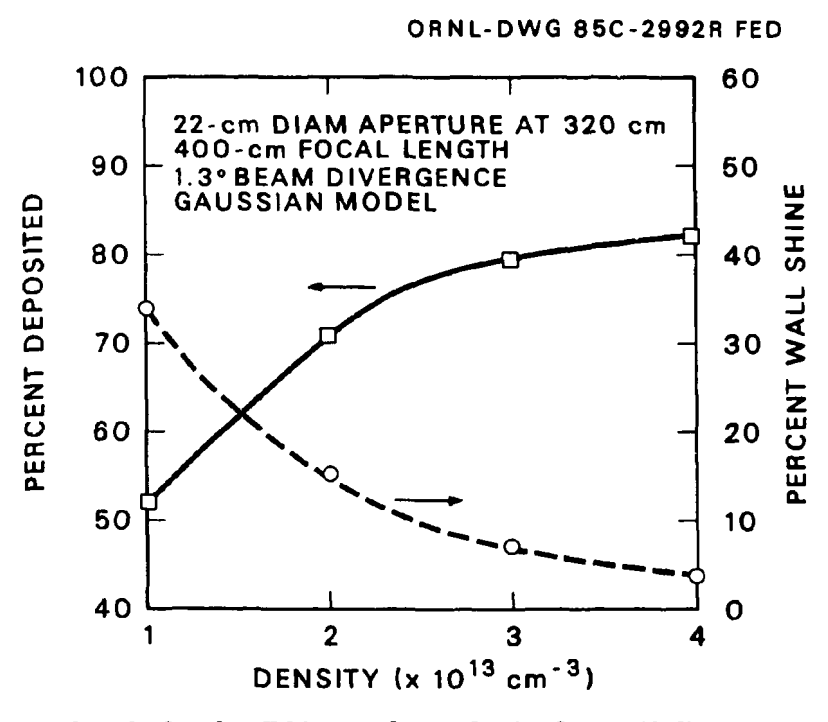


Fig. 13. Power deposited and wallshine vs plasma density for a 1.3° divergence, 400-cm focal length beam.

The beam modeling thus far has been done using a Gaussian model for the beam profile; in experimental work a much slower decay of the wings of the beam is noted, and a study was undertaken to determine if this was an important effect. The beam profile from Ref. 9 was modeled as shown in Fig. 14. The markers are data points, the dashed line is the 1.3° divergence Gaussian model used in the previous parts of this work. The dotted line is a 1.1° divergence Gaussian, and the solid line, the following normalized bi-Gaussian fit:

$$I = A \exp \left[-\left(\Delta/a\right)^{2}\right] + B \exp \left[-\left(\Delta/b\right)^{2}\right] ,$$

where A = 0.08529, B = 0.9147, a = 0.05744, b = 0.01791, and  $\Delta$  is the geometric distance function (see Appendix B). Note that the 1.3° Gaussian attempts to model the tails of the beam distribution peak and that the 1.1° divergence Gaussian models the peak at the expense of the tails.

Since the injector on which measurements were made in Ref. 9 is similar to the ISX-B injector, there was concern that the tails would cause additional wall loading. Figure 15 shows the power

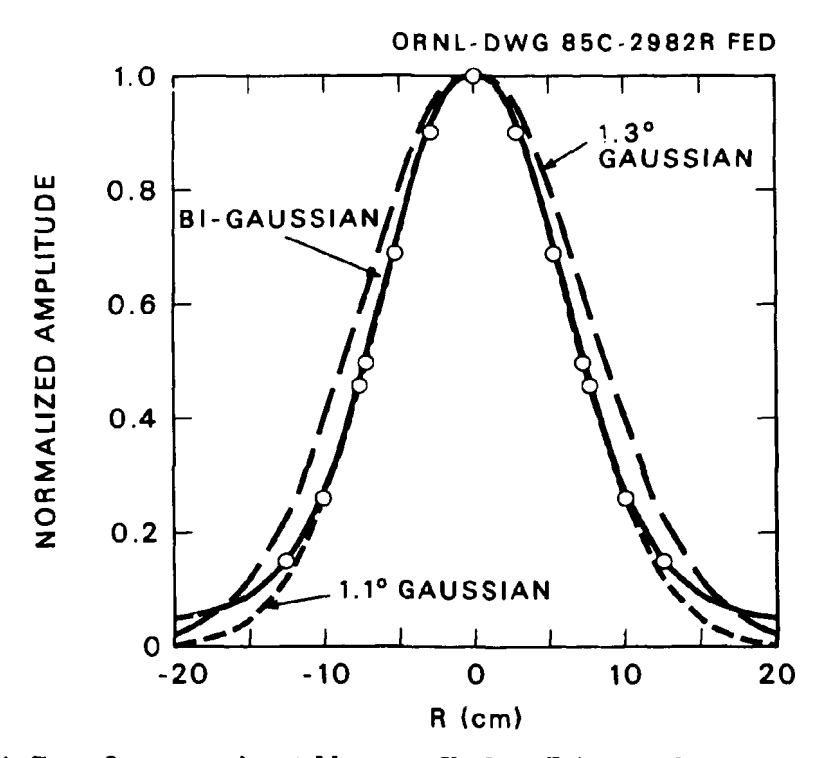


Fig. 14. Curve fits to experimental beam profile data. Points are data, solid line is bi-Gaussian fit, dashed line is 1.3° divergence Gaussian, and dotted line is 1.1° divergence Gaussian fit. R is the radius in cm from the center of the target, and AMP is the relative amplitude.

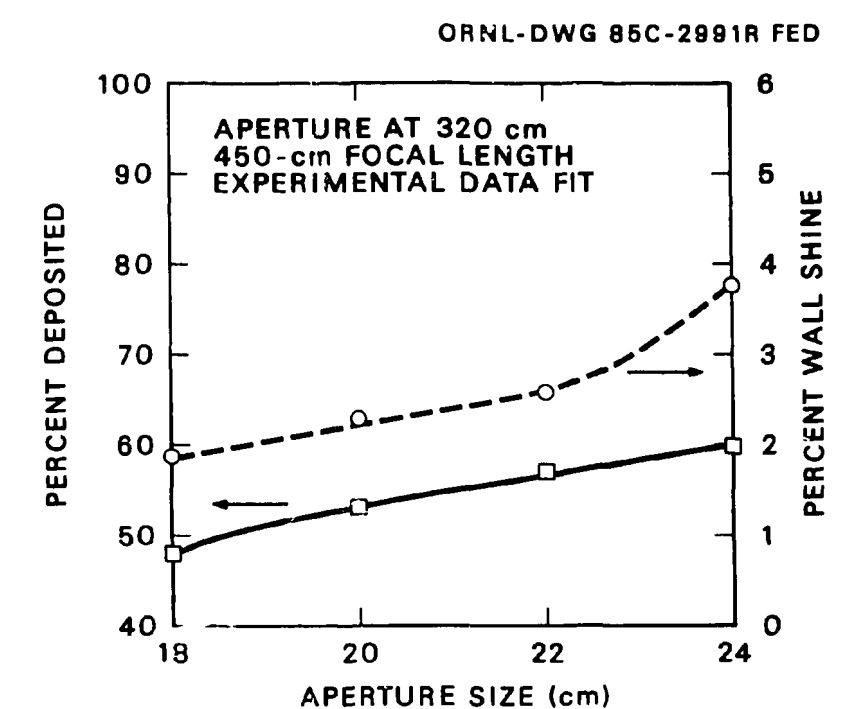


Fig. 15. Power deposited and wallshine vs aperture size for an experimentally measured beam profile.

deposition and wallshine for the bi-Gaussian model as a function of aperture diameter. With no aperture the beam will hit the port and duct, but with an aperture the troublesome particles are removed. Note that because of the long distribution tail the aperture must intercept a much larger portion of the incident beam power, significantly reducing the power available to heat the plasma. This beam model, in general, provides a more pessimistic result than the Gaussian model. This is to be expected for any model that places significant beam energy at large divergence angles. Table 1 provides a comparison of the experimental and Gaussian models. Even the experimental model should achieve the design goal of 1.5 MW into the plasma, which is as good as the maximum performance obtained from the ISX-B beams.

Table 1. Power into plasma

Aperture	Model	Experiment					
18 cm diam	1.9 MW	1.3 MW					
20 cm	2.1 MW	1.4 MW					
22 cm	2.2 MW	1.5 MW					
24 cm	2.3 MW	1.6 MW					

Power to source

4.0 MW

Power into beam: 2.7 MW

Model:

1.3°, 400-cm focal

length Gaussian

distribution.

Experiment:

Data fit to Ref. 9.

### 4. FAST-ION CONFINEMENT

A preliminary calculation of the energy delivered to the plasma ions and electrons has been made with a Monte Carlo transport code.<sup>10</sup> The energy loss due to fast-ion orbits leaving the plasma is also computed. The governing equation used for the fast-ion slowing-down process is

$$dv/dt = -\left(v_0^3 + v_0^3\right)/\tau_0 v_0^2 ,$$

where  $\tau_s$  is the Spitzer ion-electron momentum exchange time and  $v_c$  is the speed associated with the critical energy. A pitch angle scattering operator is applied in a fashion similar to that used by Boozer and Kuo-Petravic. For comparison, the energy transferred to the plasma ions and electrons is also computed from the moments  $G_i$  and  $G_c$  of the fast-ion Folker-Planck equation to see if they can be applied as useful approximations in special cases. In all cases the fast-ion losses are less than 10% of the energy delivered to the plasma. The  $G_c$  and  $G_i$  moments are in reasonable agreement with the results obtained from the particle-following computations, even though the moments analysis does not strictly apply in a stellarator geometry. The agreement is most likely based on the fact that only a small fraction of the injected ions are deposited on trapped particle orbits because of the tangential injection used in ATF. Results are shown in Figs. 16 and 17. The plasma parameters used in this study are:

$$n_i = n_e = n_0 (1 - \psi) + n_t$$
,  
 $T_i = T_e = T_0 (1 - \psi) + T_t$ ,  
 $\Phi = \Phi_0 (1 - \psi)$ ,

where the density, temperature, and electric potential parameters are:  $n_0 = 4 \times 10^{12}$  cm<sup>-3</sup>,  $n_t = 1 \times 10^{12}$  cm<sup>-3</sup>,  $T_0 = 1$  keV,  $T_t = 0.05$  keV, and  $\phi_0 = 2$  kV. The flux surface label  $\psi$  is normalized between 0 and 1.

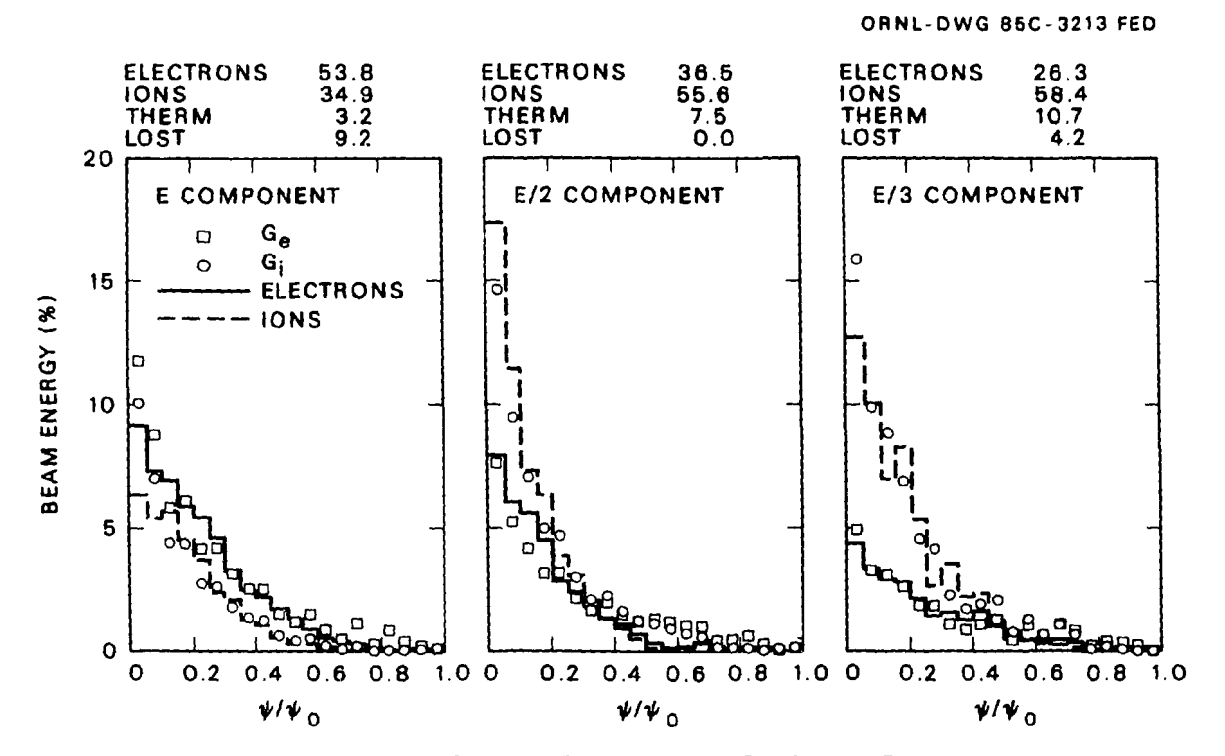


Fig. 16. Total energy deposition from fast ions vs flux surface.

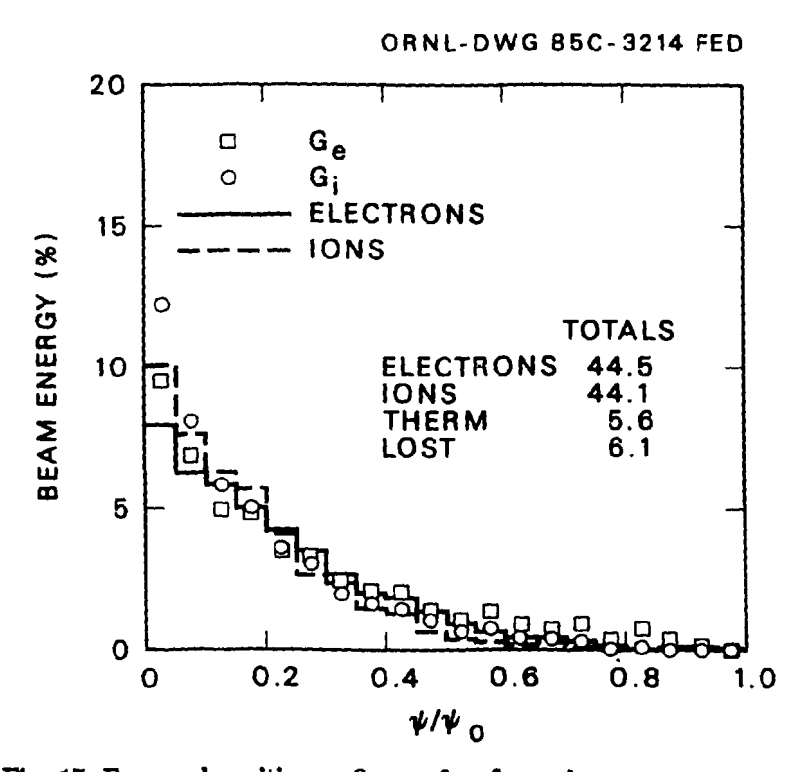


Fig. 17. Energy deposition vs flux surface for each energy component.

## 5. CONCLUSIONS

The current model for neutral beam injection into ATF shows that the design goal of 1.5 MW deposited in the plasma can be achieved. This is the case even with the bi-Gaussian model with significant beam aperturing, currently the most pessimistic model. In all cases a beam aperture will be required to prevent the beam from striking the beam duct and vacuum vessel port, in addition to holding the wallshine to manageable levels. If modification of the beam line is desired, the most important parameter to improve is the beam divergence.

Beam modeling indicates that large differences in the power deposited within the plasma can occur, depending on the details of the beam model used. This fact points to the need to obtain beam data relevant to the particular injector used for the experiment.

Finally, first results from the fast-ion loss analysis indicate that the fast-ion losses will be small.

### REFERENCES

- 1. G. G. Lister, D. E. Post, and R. Goldston, "Computer Simulation of Neutral Beam Injection into Tokamaks Using Monte Carlo Techniques," p. 303 in Proceedings of the Third International Symposium on Plasma Heating in Toroidal Devices, Varenna, Italy, 1976.
- 2. R. H. Fowler, J. A. Holmes, and J. A. Rome, "NFREYA A Monte Carlo Beam Deposition Code for Noncircular Tokamak Plasmas," ORNL/TM-6845, Oak Ridge National Laboratory, 1979.
- S. A. Hokin, J. A. Rome, T. C. Hender, R. H. Fowler, "Neutral Beam Heating in Stellarators: A Numerical Approach," ORNL/TM-8530, Oak Ridge National Laboratory, 1983.
- M. J. D. Powell, "A Hybrid Method for Nonlinear Algebraic Equations," in Numerical Methods of Nonlinear Algebraic Equations, E. P. Rabinowitz, ed., Gordon and Breach, New York, 1970.
- J. J. More, B. S. Garbow, and K. E. Hillstrom, User Guide for MINPACK-1, ANL-80-74, Argonne National Laboratory, 1980.
- 6. A. H. Boozer, "Guiding Center Drift Equations," Phys. Fluids 28, 904 (1980).
- G. Kuo-Petravic, A. H. Boozer, J. A. Rome, and R. H. Fowler, "Numerical Evaluation of Magnetic Coordinates for Particle Transport Studies in Asymmetric Plasmas," J. Comput. Phys. 51, 261 (1983).
- W. M. Rohsenow and J. P. Hartnett, Handbook of Heat Transfer, McGraw Hill Book Company, New York, 1973.
- 9. W. L. Gardner et al., "Properties of an Intense 50-kV Neutral-Beam Injection System," Rev. Sci. Instrum., 53, 424 (1982).
- R. H. Fowler, J. A. Rome, and J. F. Lyon, "Monte Carlo Studies of Transport in Stellarators," Phys. Fluids 28, 338 (1985).
- 11. J. D. Callen et al., "Neutral Beam Injection into Tokamaks," p. 645 in Proceedings of the Fifth International Conference on Plasma Physics and Controlled Nuclear Fusion Research, vol. 1, Tokyo, Japan, 1975.
- 12. A. H. Boozer and G. Kuo-Petravic, "Monte Carlo Evaluation of Transport Coefficients," *Phys. Fluids* 24, 851 (1981).

## ABSTRACT

The application of the existing Impurity Study Experiment (ISX-B) neutral beam injectors for the Advanced Toroidal Facility (ATF) is studied. It is determined that with the practical considerations of beam aperturing, ATF vacuum vessel complexity, and realistic beam modeling, the power absorbed by the plasma will be approximately 57% of the extracted neutral beam power, which corresponds to an injected power of about 1.5 MW. By reducing the beam divergence to a 1° Gaussian distribution, the absorbed power could be increased to 93%. The power delivered to the plasma is found to be a strong function of the beam divergence but only a weak function of the beam focal length. Shinethrough can be a serious problem if very low density startups are necessary. Preliminary calculations indicate that there will be no excessive fast-ion losses.

# APPENDIX A COORDINATE MAPPING

The conversion from Cartesian coordinates to Boozer coordinates is accomplished by solving a set of nonlinear equations, using the hybrid Newton's method contained in the NAG subroutine C05PBF. For specific details, the interested reader is referred to Refs. A1 and A2.

The Boozer flux coordinate representation is:

$$r = \sum r_{mn}(\psi) \cos(n\phi - m\theta)$$
,  
 $z = \sum z_{mn}(\psi) \sin(n\phi - m\theta)$ ,  
 $\Phi = \sum \Phi_{mn}(\psi) \sin(n\phi - m\theta) + \phi$ ,

where  $\psi$ ,  $\theta$ , and  $\phi$  are the Boozer coordinates;  $r_{mn}$ ,  $z_{mn}$ , and  $\Phi_{mn}$  are the flux surface harmonic functions; A3 and r, z, and  $\Phi$  are the known real-space coordinates.

Experience indicates that approximately 90% of the time, the numerical subroutine will converge to the correct answer by using the following initial values for the Boozer variables:

$$\psi = 0.25\psi_{
m max} \; ,$$
  $heta = an^{-1} \left[ z/\left(r-r_a
ight) 
ight] \; ,$   $\phi = \Phi \; ,$ 

where  $r_a$  is the magnetic axis and  $\psi_{max}$  is the maximum value of  $\psi$  (known).

If convergence is not obtained on the first pass, the starting value for  $\psi$  is decreased to a value near but greater than 0, and the subroutine is called again. If this fails, the subroutine is called at least twice more with starting values for  $\psi$  near the half-way point and finally near  $\psi_{\text{max}}$ . A maximum of four attempts is made to obtain convergence. In all cases observed to date, convergence has been obtained, provided that the harmonic functions of the Boozer coordinate expansions are modified to have a linear functional form when  $\psi$  exceeds  $\psi_{\text{max}}$ . This ensures that points outside the plasma will be mapped to a value of  $\psi$  that exceeds  $\psi_{\text{max}}$  and thus will be outside the plasma as required.

In practice the r, z, and  $\Phi$  harmonics are computed on a numeric grid, and a least-squares polynomial is fit to the computed data. It is best to factor out the asymptotic behavior near the origin to ensure the best functional representation for the harmonic functions. In that light, the following form is used in the computations:

$$X_{mn} = A(\psi)P(\psi) .$$

 $A(\psi)$  is an asymptotic functional form to ensure that the harmonics have the proper form near  $\psi = 0$ . It is of the form  $\psi^{m/2} \exp\left[-m\psi/(2\psi_{\text{max}})\right]$ , with the absolute value of m used for negative m.  $P(\psi)$  is a least-squares fitted polynomial.

A short note of the fitting of the polynomial is in order because of the non-trivial nature of the operation. The harmonic functions are computed by numerical integration at discrete points; for small values of  $\psi$  they are very small and may be in error. To curve fit the function well it is necessary first to filter out the bad and spurious points to ensure that the resulting polynomial does not exhibit wild and unpredictable behavior. This process, unfortunately, appears to have a large heuristic component because of the unknown nature of the spurious points and noise. It is recommended that the resulting curve fits be graphed before use so that representative curve fits can be confirmed. Spline fits are also possible provided that the user filters out all the bad points; it also may be troublesome to generate the proper asymptotic form near  $\psi = 0$ .

### REFERENCES FOR APPENDIX A

- A1. M. J. D. Powell, "A Hybrid Method for Nonlinear Algebraic Equations," in Numerical Methods of Nonlinear Algebraic Equations, E. P. Rabinowitz, ed., Gordon and Breach, New York, 1970.
- A2. J. J. More, B. S. Barbow, and K. E. Hillstrom, User Guide for MINPAK-1, ANL-80-74, Argonne National Laboratory, 1980.
- A3. G. Kuo-Petravic, A. H. Boozer, J. A. Rome, and R. H. Fowler, "Numerical Evaluation of Magnetic Coordinates for Particle Transport Studies in Asymmetric Plasmas," J. Comput. Phys. 51, 261 (1983).

# APPENDIX B BEAM MODEL PHYSICS

### PARTICLE NUMBER SELECTION

In determining the number of atoms in a given beam at a given energy level, it is important to differentiate between atoms and molecules. The beam model used in this work allows three species to enter the neutralizer,  $H_1^+$ ,  $H_2^+$ ,  $H_3^+$ , in the form of singly charged molecules. As they exit from the neutralizer they are all in the form of atomic hydrogen. Since all species are accelerated through the same electric field, the current due to any one species is:

$$I_i = Ap_i eV_i$$
.

where  $p_i$  is the number of molecules accelerated per species; it is equal to  $n_i/\delta_i$ , where  $n_i$  is the number of atoms per species, and  $\delta_i$  is the number of atoms per molecule (i, 2, or 3). The electric charge is e,  $V_i$  the velocity of the *i*th species,  $V_i = (2eE_0/\delta_i m)^{1/2}$ , m is the mass of the atom, A is the cross-sectional area of the beam, and  $E_0$  is the applied electric field.

The total current is the sum of the individual currents,

$$I_1 + I_2 + I_3 = I_0$$
.

With the only species being  $H_1^+$ ,  $H_2^+$ , and  $H_3^+$ , the currents may be written as (note that  $\delta_1 = 1$ ,  $\delta_2 = 2$ ,  $\delta_3 = 3$ ):

$$I_1 = C_0 n_1 = f_1 I_0$$

$$I_2 = C_0 n_2 / (2\sqrt{2}) = f_2 I_0$$

$$I_3 = C_0 n_3 / (3\sqrt{3}) = f_3 I_0$$

where  $C_0$  is a constant incorporating all the fixed parameters, and  $f_i$  represents the fraction of the total source current.

The power in any individual species is:

$$P_i = I_i E_0$$
.

The total power is

$$P_t = \sum P_i = I_0 E_0 (f_1 + f_2 + f_3) ,$$

giving

$$f_1 + f_2 + f_3 = 1.$$

To compute the particle numbers used in the simulation, one needs to know the efficiency  $\eta_i$  of the neutralizer for a given energy and the total number of particles  $\eta_i$  that leave the neutralizer:

$$\eta_1 n_1 + \eta_2 n_2 + \eta_3 n_3 = n_t$$
.

Using the expression for the currents in the above equation yields a relationship for  $n_i$  and  $C_0$  which can be cast into the following form for  $n_i$ :

$$n_i = \left(n_t f_i i^{3/2}\right) / \left(\eta_i f_i + 2\sqrt{2}\eta_2 f_2 + 3\sqrt{3}\eta_3 f_3\right) , \quad i = 1, 2, 3.$$

In general the Monte Carlo simulation follows only a small portion of the total particles  $N_t$ , so that one sets

$$S = n_t/N_t$$
,

and

$$N_1 + N_2 + N_3 = N_t ,$$

where  $N_i = \eta_i n_i / S$ , and  $N_i$  is the actual number of particles used.

#### WALL HEATING AND SPUTTERING

A simple model is used to provide an estimate of the total wall sputtering yield and energy deposition.

The total number of particles per second per species is:

$$p_i = P_i/\varepsilon_i$$
,

where  $p_i$  is the number of neutral beam atoms per second per species that leave the neutralizer,  $P_i$  is the total power per species in watts after neutralization, and  $e_i$  is the energy per particle per species in joules. Each code pseudo particle represents  $p_i/N_i$  real particles ( $N_i$  is the number of pseudo particles per energy group). Thus each time a pseudo particle hits the wall, the energy of the appropriate number of real particles is tallied up to the total to compute the wall loading. The

sputtering yield is computed by multplying  $p_i/N_i$  by the sputter fraction per incident neutral. The sputtering process assumes no angle dependence and thus provides a crude estimate of the total sputtering.

#### VELOCITY DISTRIBUTION FUNCTION

The velocity distribution function of the perpendicular velocity of a beam particle that models the experimental data is of the form:

$$f(\theta) = f_1 \theta \exp\left(-\theta^2/\theta_1^2\right) + f_2 \theta \exp\left(-\theta^2/\theta_2^2\right) ,$$

where  $\theta$  is the angle between the emitted particle and the optical axis of the source and  $\theta_1$ ,  $\theta_2$ ,  $f_1$ , and  $f_2$  are constants determined by the beam test data. A practical beam source is assumed to be made up of a large number of such emitters, each aimed at the beam focal point. The beam intensity profile is usually measured at the beam focal point, where it is assumed that all the point source emitters are aimed. At this point the beam intensity profile is the same as that of the point source emitters, and experimental measurements can be performed to find the above beam parameters.

To see that  $f(\theta)$  represents the test data, refer to Fig. B1. Assume that the source is located far from the target so that R >> r and  $\tan(\theta) \approx \theta \approx r/R$ . Furthermore, assume only a functional dependence on r. Then from Fig. B1:

$$2\pi r dr I(r) \approx \int_{\theta}^{\theta+d\theta} \int_{0}^{2\pi} d\theta d\phi f(\theta)$$
.

Integrating in  $\phi$  and using the small-angle approximations for  $\theta$  yields

$$I(r)r dr \approx \int_{r/R}^{(r+dr)/R} f(\theta) d\theta$$
,

where I(r) is the source intensity on the target. After evaluating the integral and approximating the exponential terms containing dr by their Taylor series expansions, one gets for the point source emitter or for the beam intensity at the focal point: $^{B1,B2}$ 

$$I(r) = \left\{ f_1 \exp \left[ -(r/R\theta_1)^2 \right] + f_2 \exp \left[ -(r/R\theta_2)^2 \right] \right\} / R^2$$
.

The probability distribution function,  $P(\theta)$ , is the normalized integral of the velocity distribution function,

$$P(\theta) = \int_0^{\theta} f(\theta) \ d\theta / \int_0^{\infty} f(\theta) \ d\theta \ .$$

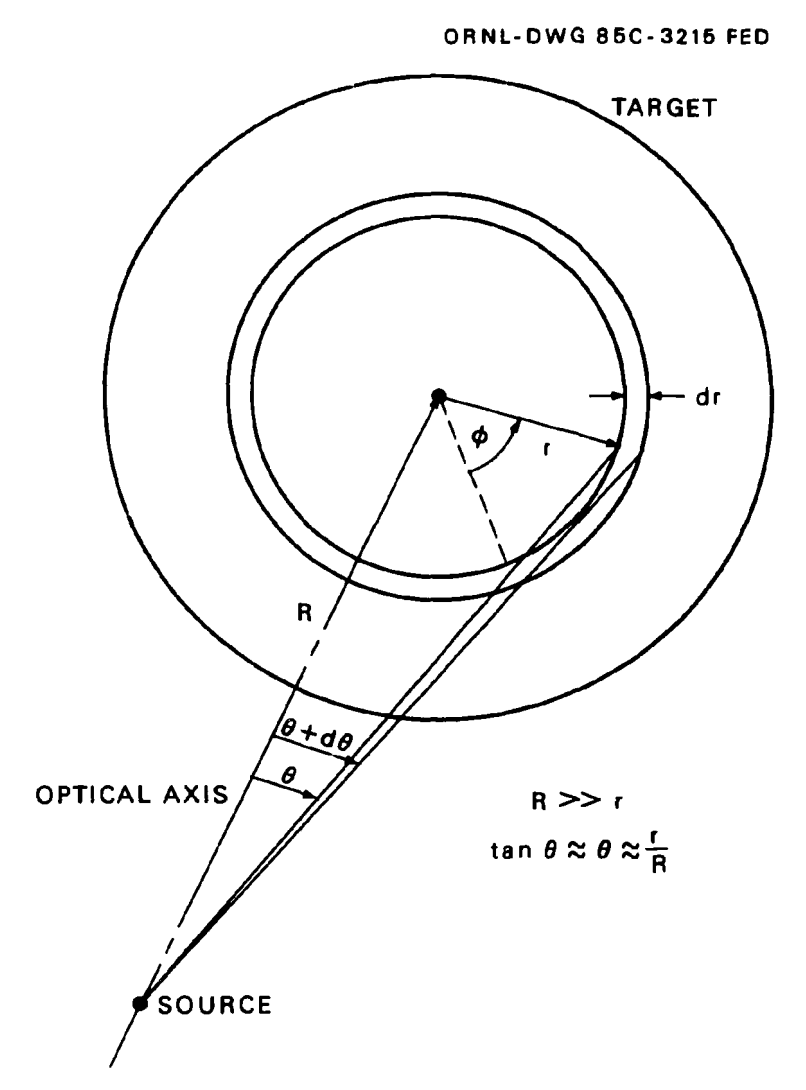


Fig. B1. Schematic view of point beam source and target.

Performing the integration one gets

$$R = \left[ f_1 \theta_1^2 \exp(-\theta^2/\theta_1^2) + f_2 \theta_2^2 \exp(-\theta^2/\theta_2^2) \right] / (f_1 \theta_1^2 + f_2 \theta_2^2) ,$$

where R, a random number between zero and one, is equal to  $1 - P(\theta)$ .

With  $f_1 = 1$  and  $f_2 = 0$ , we get the simple Gaussian model, which forms the basis for most of the work in the field. In this case  $\theta_1$  is a measure of the beam divergence. With  $f_1 = 0$  and  $f_2 = 0$ , we get the bi-Gaussian model, which offers greater flexibility in modeling beam intensity profiles with a slowly decaying tail.

# REFERENCES FOR APPENDIX B

- B1. W. L. Gardner et al., "Properties of an Intense 50-kV Neutral-Beam Injection System," Rev. Sci. Instrum. 53, 424 (1982).
- B2. J. Kim and J. H. Whealton, "Beam Intensity Distributions in Neutral Beam Injection Systems," Nucl. Instrum. Meth. 14, 187 (1977).

- 83. Theory Department Read File, c/o C. S. Liu, GA Technologies, Inc., P.O. Box 81608, San Diego, CA 92138
- 84. Theory Department Read File, c/o L. D. Pearlstein, Lawrence Livermore National Laboratory, P.O. Box 808, Livermore, CA 94550
- 85. Theory Department Read File, c/o R. Gerwin, CTR Division, Los Alamos National Laboratory, P.O. Box 1663, Los Alamos, NM 87545
- 86. R. E. Mickens, Department of Physics, Atlanta University, Atlanta, GA 30314
- 87. C. De Palo, Library, Associazione EURATOM-ENEA sulla Fusione, CP 65, I-00044 Frascati (Roma), Italy
- 88-243. Given distribution as shown in TIC-4500 Magnetic Fusion Energy (Category Distribution UC-20 g: Theoretical Plasma Physics)

### ORNL/TM-9689

Dist. Category UC-20 g

#### INTERNAL DISTRIBUTION

1. L. A. Berry
2. R. A. Dory
3. P. H. Edmonds
4. R. D. Foskett
5. R. H. Fowler
6. H. C. Howe
7. T. C. Jernigan
8. J. F. Lyon
9. M. M. Menon
10. P. K. Mioduszewski
11–15. R. N. Morris
16. G. H. Neilson

17. Y-K. M. Peng

18-22. J. A. Rome
23. M. J. Saltmarsh
24. J. Sheffield
25. W. I. van Rij
26. G. E. Whitesides
27-28. Laboratory Records Department
29. Laboratory Records, ORNL-RC
30. Document Reference Section
31. Central Research Library
32. Fusion Energy Division Library

33-34. Fusion Energy Division Publications Office 35. ORNL Patent Office

### **EXTERNAL DISTRIBUTION**

- 36. P. H. Diamond, Institute for Fusion Studies, University of Texas at Austin, Austin, TX 78712
- 37. Office of the Assistant Manager for Energy Research and Development, Department of Energy, Oak Ridge Operations Office, P.O. Box E, Oak Ridge, TN 37831
- 38. J. D. Callen, Department of Nuclear Engineering, University of Wisconsin, Madison, WI 53706
- 39. R. W. Conn, Department of Chemical, Nuclear, and Thermal Engineering, University of California, Los Angeles, CA 90024
- 40. S. O. Dean, Director, Fusion Energy Development, Science Applications International Corp., Gaithersburg, MD 20760
- 41. H. K. Forsen, Bechtel Group, Inc., Research Engineering, P.O. Box 3965, San Francisco, CA 94205
- 42. J. R. Gilleland, GA Technologies, Inc., Fusion and Advanced Technology, P.O. Box 85608, San Diego, CA 92138
- 43. R. W. Gould, Department of Applied Physics, California Institute of Technology, Pasadena, CA 91125
- 44. R. W. Gross, Plasma Research Library, Columbia University, New York, NY 10027
- 45. D. M. Meade, Princeton Plasma Physics Laboratory, P.O. Box 451, Princeton, NJ 08544
- 46. W. M. Stacey, School of Mechanical Engineering, Georgia Institute of Technology, Atlanta, GA 30332
- 47. D. Steiner, Rensselaer Polytechnic Institute, Troy, NY 12181
- 48. R. Varma, Physical Research Laboratory, Navrangpura, Ahmedabad 380009, India
- 49. Bibliothek, Max-Planck Institut für Plasmaphysik, D-8046 Garching, Federal Republic of Germany
- 50. Bibliothek, Institut fur Plasmaphysik, KFA, Postfach 1913, D-5170 Julich, Federal Republic of Germany
- 51. Bibliotheque, Centre des Recherches en Physique des Plasmas, 21 Avenue des Bains, 1007 Lausanne, Switzerland
- 52. Bibliotheque, Service du Confinement des Plasmas, CEA, B.P. No. 6, 92 Fontenay-aux-Roses (Seine), France
- 53. Documentation S. I. G. N., Department de la Physique du Plasma et de la Fusion Controlee, Centre d'Etudes Nucleaires, B.P. 85, Centre du Tri, 38081 Cedex, Grenoble, France

- 54. Library, Culham Laboratory, UKAEA, Abingdon, Oxfordshire, OX14 3DB, England
- 55. Library, FOM-Instituut voor Plasma-Fysica, Rijnhuizen, Edisonbaan 14, 3439 MN Nieuwegein, The Netherlands
- 56. Library, Institute of Plasma Physics, Nagoya University, Nagoya, Japan
- 57. Library, International Centre for Theoretical Physics, Trieste, Italy
- 58. Library, Laboratorio Gas Ionizatti, CP 56, I-00044 Frascati (Roma), Italy
- Library, Plasma Physics Laboratory, Kyoto University, Gokasho, Uji, Kyoto, Japan
- Plasma Research Laboratory, Australian National University, P.O. Box 4, Canberra, A.C.T. 2000, Australia
- Thermonuclear Library, Japan Atomic Energy Research Institute, Tokai, Naka, Ibaraki, Japan
- G. A. Eliseev, I. V. Kurchatov Institute of Atomic Energy, P.O. Box 3402, 123182 Moscow, U.S.S.R.
- 63. V. A. Glukhikh, Scientific-Research Institute of Electro-Physical Apparatus, 188631 Leningrad, U.S.S.R.
- 64. I. Shpigel, Institute of General Physics, U.S.S.R. Academy of Sciences, Ulitsa Vavilova 38, Moscow, U.S.S.R.
- 65. D. D. Ryutov, Institute of Nuclear Physics, Siberian Branch of the Academy of Sciences of the U.S.S.R., Sovetskaya St. 5, 630090 Novosibirsk, U.S.S.R.
- V. T. Tolok, Kharkov Physical-Technical Institute, Academical St. 1, 310108 Kharkov, U.S.S.R.
- 67. Library, Institute of Physics, Academia Sinica, Beijing, Peoples Republic of China
- 68. J. F. Clarke, Associate Director for Fusion Energy, Office of Fusion Energy, ER-50, Germantown, U.S. Department of Energy, Washington, DC 20545
- D. B. Nelson, Division of Applied Plasma Physics, Office of Fusion Energy, Office of Energy Research, ER-54, Germantown, U.S. Department of Energy, Washington, DC 20545
- 70. N. A. Davies, Tokamak Systems Branch, Office of Fusion Energy, Office of Energy Research, ER-55, Germantown, U.S. Department of Energy, Washington, DC 20545
- 71. E. Oktay, Tokamak Systems Branch, Office of Fusion Energy, Office of Energy Research, ER-55, Germantown, U.S. Department of Energy, Washington, DC 20545
- 72. Theory Department Read File, c/o D. W. Ross, University of Texas, Institute for Fusion Studies, Austin, TX 78712
- 73. Theory Department Read File, c/o R. C. Davidson, Director, Plasma Fusion Center, NW 16-202, Massachusetts Institute of Technology, Cambridge, MA 02139
- Theory Department Read File, c/o F. W. Perkins, Princeton Plasma Physics Laboratory, P.O. Box 451, Princeton, NJ 08544
- Theory Department Read File, c/o L. Kovrizhnykh, Institute of General Physics, Academy of Sciences of the U.S.S.R., Ulitsa Vavilova 38, Moscow, U.S.S.R.
- Theory Department Read File, c/o B. B. Kadomtsev, I. V. Kurchatov Institute of Atomic Energy, P.O. Box 3402, 123182 Moscow, U.S.S.R.
- 77. Theory Department Read File, c/o T. Kamimura, Institute of Plasma Physics, Nagoya University, Nagoya, Japan
- 78. Theory Department Read File, c/o C. Mercier, Euratom-CEA, Service des Recherches sur la Fusion Controlee, Fontenay-aux-Roses (Seine), France
- 79. Theory Department Read File, c/o T. E. Stringer, JET Joint Undertaking, Culham Laboratory, Abingdon, Oxfordshire OX14 3DB, England
- 80. Theory Department Read File, c/o K. Roberts, Culham Laboratory, Abingdon, Oxfordshire OX14 3DB, England
- 81. Theory Department Read File, c/o D. Biskamp, Max-Planck-Institut fur Plasmaphysik, D-8046 Garching, Federal Republic of Germany
- 82. Theory Department Read File, c/o T. Takeda, Japan Atomic Energy Research Institute, Tokai, Naka, Ibaraki, Japan